A Vision-Based Technique for Objective Assessment of Burn Scars

Leonid V. Tsap,* *Student Member, IEEE*, Dmitry B. Goldgof, *Senior Member, IEEE*, Sudeep Sarkar, *Member, IEEE,* and Pauline S. Powers

Abstract—In this paper a method for the objective assessment of burn scars is proposed. The quantitative measures developed in this research provide an objective way to calculate elastic properties of burn scars relative to the surrounding areas. The approach combines range data and the mechanics and motion dynamics of human tissues. Active contours are employed to locate regions of interest and to find displacements of feature points using automatically established correspondences. Changes in strain distribution over time are evaluated. Given images at two time instances and their corresponding features, the finite element method is used to synthesize strain distributions of the underlying tissues. This results in a physically based framework for motion and strain analysis. Relative elasticity of the burn scar is then recovered using iterative descent search for the best nonlinear finite element model that approximates stretching behavior of the region containing the burn scar. The results from the skin elasticity experiments illustrate the ability to objectively detect differences in elasticity between normal and abnormal tissue. These estimated differences in elasticity are correlated against the subjective judgments of physicians that are presently the practice.

Index Terms—Biomedical applications, deformable models, finite element analysis, iterative descent algorithm, nonrigid motion analysis, physically based vision.

I. INTRODUCTION

A. Motivation

IN computer vision, motion analysis is a field of intensive research. Although the motion of some objects can be approximated with the rules of rigid motion, in most cases physical entities move nonrigidly. There is no elegant rule to describe this kind of motion. However, the demand for nonrigid motion estimation algorithms is great, especially from sciences that are studying the behavior of human body parts, such as medical imaging (including cardiac motion, hand, and knee modeling), face and gesture recognition, and videoconferencing. To describe nonrigid motion, it is logical to employ the laws of rigid and nonrigid dynamics expressed through a set of Lagrangian equations that govern this motion. For this reason,

*L. V. Tsap is with the Department of Computer Science and Engineering, University of South Florida, Tampa, FL 33620 USA (e-mail: tsap@csee.usf.edu).

D. B. Goldgof and S. Sarkar are with the Department of Computer Science and Engineering, University of South Florida, Tampa, FL 33620 USA.

P. S. Powers is with the Department of Psychiatry/Tampa Bay Regional Burn Center, University of South Florida, Tampa, FL 33620 USA.

physically based models are unrivaled in modeling complex local deformations. Nonlinear FEM allows modeling of both material nonlinearities in the form of nonlinear properties and geometric nonlinearities in the form of large deformations.

In this paper, computer vision is applied to the problem of burn scar assessment. In the United States, two million people are burned annually; 300 000 cases are considered serious [1]. Scars, which appear as products of successful wound healing, differ from normal skin in several important ways, including the color, texture, size, and shape. Scars also change over time, especially during the first 18 months after initial healing. Along with advances in the understanding of the process of scar formation, recent years have seen progress in the therapeutic treatment of scars. Treatment procedures include using various types of pressure garments, drugs, or even surgery. Despite various new developments in terms of reducing scars or their impact, the ability to *objectively* assess scars is still very limited. In the interest of making the best choice for the patient, various healing techniques must be compared and contrasted both subjectively and objectively. Patients' own subjective assessment of their scars may be one of the factors influencing function both at work and socially. This paper presents a set of algorithms for objectively determining elastic properties of burn scars relative to the surrounding areas. Such properties not only define the objective parameters of the scar, but also the success of the healing process [2].

These algorithms are applied to images of burn scars, and evaluated against judgments of the specialists participating in this research, W. C. Cruse and T. S. Krizek from Tampa Bay Regional Burn Center, and P. S. Powers from the Department of Psychiatry/Tampa Bay Regional Burn Center. The Burn Center is the part of the American Burn Association Burn Registry. The number of patients accepted per year: 754 admissions, 720 initial admissions [1]. These specialists use a scale similar to Vancouver Scar Assessment Technique to rate characteristics of burn scars. The problem with this scale is the low reliability of measurements (when two or more physicians do not get the same results). Repeatability is also a problem because the same specialist may not access a scar the same way twice. That is why the long-term goal of this research is to evaluate different burn scar treatment procedures armed with objective measures of the scar that our research allows to achieve and adjust treatment strategies accordingly.

B. Previous Work

This section presents a short review of the previous work in related areas. The methodology described in this paper

draws from a diverse body of knowledge. First, the work in computer vision related to physically based modeling and active contours is addressed. Second, research in the area of burn scar assessment is shown. Third, a review of research in the field of biomechanical characterization of skin is presented.

1) Computer Vision:

a) Physically based modeling: In computer vision, physically based modeling is used most often for three-dimensional (3-D) shape fitting and motion analysis. Terzopoulos and Metaxas [3] presented a physically based approach to shape modeling that simultaneously satisfies the requirements of reconstruction and recognition. A paper by Yamamoto *et al.* [4] described a truly pioneering work in nonrigid motion analysis utilizing both intensity and range data. They proposed a deformable net model consisting of nodes and links, which allowed (similar to the grid in the experiments conducted in this research) the estimation of deformable motion parameters by establishing correspondences between images in a sequence. DeCarlo and Metaxas [5] proposed to incorporate blending into deformable models. Neuenschwander *et al.* [6] defined deformable surfaces using elastic model representation such as triangulated meshes. Sclaroff and Pentland [7] used FEM to obtain a parametric description of nonrigid motion in terms of its similarity to known extrenal views. Young and Axel [8] built a finite element model of the left ventricle to fit material points tracked in biplanar views. Metaxas and Koh [9] used local adaptive finite elements to represent 3-D shapes efficiently. Davis *et al.* [10] designed the elastic body spline (EBS) to approximate behavior of a homogeneous, isotropic, elastic material subjected to a load. The EBS was applied to matching 3-D magnetic resonance images (MRI's) used in the evaluation of breast cancer. A finite element model that learns the correct physical model of human lips by training from real data was proposed by Basu and Pentland [11]. Huang, Goldgof [12], [13], and Tsap *et al.* [14], [15] first suggested the use of nonlinear FEM for nonrigid motion analysis.

b) Active contours: Active contour models, or snakes, were first introduced by Kass *et al.* [16] as a mechanism for finding and tracking salient image contours. Terzopoulos and Waters [17], [18] developed snakes to track the nonrigid motions of facial features in video images. Leymarie and Levine [19] used snakes with an improved terminating criterion to track deformable (nonrigid) objects in a noisy intensity image. Kumar and Goldgof [20] used active contours (snakes) to track the tagged grid in Cardiac MR images automatically. Generalization of the snake model known as *balloons* was applied by Cohen and Cohen in [21] to the segmentation of 3-D MRI images. Mclnerney and Terzopoluos [22] have addressed similar problems using a slightly different balloon model based on finite elements. Cohen and Cohen [23], [24] presented a finite element method (FEM) to track a series of two-dimensional slices of heart ventricles and to make a 3-D reconstruction of the inside surface of the ventricles. Snakes continue to be in the focus of many recent models [25]–[29]. McEachen, II, and Duncan [25] tracked feature points over an entire cardiac cycle. Androutsos *et al.* [27] added image gradient direction to the energy functional and applied it to flow trace images. Yezzi *et al.* [30] unified the curve evolution approaches for active contours and the established energy formulation. Gunn and Nixon [28] used two contours to search the image space from both inside and outside of the target feature. Tagare [29] proposed a formulation that achieves reduction in the search space by precomputing orthogonal curves to deform the template. Peterfreund [31] modified active contour model by applying velocity control for real-time tracking.

2) Burn Scar Assessment: There is very little work in the area of objective assessment of burn scars. Previously, scar evaluation has been mainly subjective. Sullivan *et al.* [32] addressed the issue of a reliable, objective, and universal method of scar rating based on pigmentation, vascularity, and scar height. This approach is known as the Vancouver Scar Assessment Technique and is commonly used by plastic surgeons. However, the methodology has some subjective aspects to it, e.g., in comparing skin colors.

McHugh *et al.* [2] examined biomechanical changes after burn injury when normal skin attempts to compensate for scar contraction. The authors stressed that more precise measurements are needed to quantify these changes as well as the effects of burn scar treatment.

3) Biomechanical Skin Modeling: Another related area is the work in biomechanical properties of the skin and soft tissue. There has been a significant amount of work in characterizing the material properties of the skin and its relations to movement. The models range from plane geometric models based on continuum mechanics [33] to finite-element-based methods [34], [35]. Hyperelastic constitutive models have been shown to be appropriate to represent the material behavior of soft tissues [36]. Kallel and Bertrand [37] introduced a method to reconstruct the elastic modulus of a compressed soft tissue using simulated data. However, these techniques have not been applied to the study of burn scar recovery.

The traditional methods of quantifying biomedical properties of the skin using a tensometer are difficult to use in a clinical setting [38], [39]. Bartel *et al.* [40] described a hand-held device called the "elastometer." Traditionally, *in vivo* techniques involved the use of extensometers or elastometers under mostly uniaxial testing [40], [41]. Richard *et al.* [42] studied the relationship between joint movement and skin pliability. Larrabee and Sutton [39] used imaging techniques in the context of wound closure.

Properties of synthetic wound dressings quantified in numerous animal studies were described by Smith [43]. Other techniques include burst strength (the amount of pressure needed to rupture the tissue)—application of a strong vacuum to a small patch of the skin surface until the tissue breaks, and tensile strength testing on biopsy samples. These techniques also have been validated with animal studies for use in biomechanical research of acute wound healing [44] and have been applied to the mechanical analysis of skin equivalent models [45].

C. Overview

The hypothesis of this work is that differences in skin elasticity between normal and abnormal tissue can be recovered from observing the amount of stretching on the application
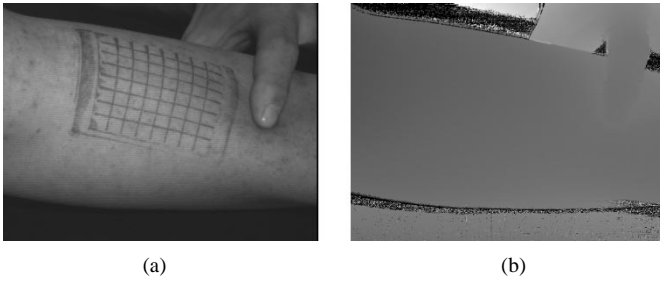
Fig. 1. Intensity and range images of the skin with the grid. Distances in the range image are encoded as intensities.

of a force. By drawing a grid pattern on the skin region of interest, the distortion of this pattern upon pulling the skin in a certain direction can be observed with the use of a range scanner. Each image sequence consists of both intensity and range images (Fig. 1) before and after the application of a force.

The grid intersections in each intensity image are detected using snakes. Such feature points from two images provide a sparse set of correspondences. The FEM is used to recover dense correspondences from the sparse data, to synthesize strain distributions of the underlying tissues and also to recover the elasticity of burn scars. Elasticity is estimated using an iterative descent search for the best nonlinear finite element model that approximates stretching behavior of the region containing the burn scar. Presented experiments show that the technique does not require the accurate knowledge of the force magnitude.

The remainder of the paper is divided into six sections (some initial results have previously appeared in [46]). Section II examines grid detection process using snakes. The approach to nonlinear finite element analysis (FEA) of skin deformations is described in Section III. Section IV presents the proposed scar assessment method. Section V demonstrates experimental results of applying the algorithm to 3-D range image sequences of burn scars. The last two sections discuss, validate, and summarize the results of this research.

II. APPLICATION OF ACTIVE CONTOURS

A. Theoretical Background

The first task is to detect automatically the grid points in two intensity images. An edge detector alone would not separate the grid from other intensity changes in the image. More prior knowledge about the grid pattern must be incorporated. The geometry of the grid, including the exact number of vertical and horizontal lines, is known in advance.

Active contour models, or snakes, allow the incorporation of such information. Snakes were first introduced by Kass *et al.* [16] as a mechanism for finding and tracking salient image contours. A snake is an energy-minimizing spline, governed by internal and external forces, and specified by a set of control points. Iterative adjustments to the snakes are made by moving the control points.

One of the fundamental qualities of snake representations is that it is possible to specify a wide range of snake properties

through an energy function. A snake evolves so as to reduce its energy; hence, the correct specification of the energy function is crucial for the success of active contours.

The energy function for a snake has two parts—the internal and external energies. The internal energy is the part that depends on intrinsic properties of the snake, such as its length or curvature. The external energy depends on factors such as image structure and particular constraints the user has imposed. The physical analogy can be extended, and the motion of the snake can be regarded as being due to simulated forces acting on it. Just as the forces on physical systems always make them move so as to reduce their energy, so the simulated forces on a snake are arranged to reduce its total energy.

Williams and Shah [47] provide a fast greedy algorithm for finding the minimum energy contour. They define the total energy of the snake as consisting of the continuity energy, the curvature energy, and the image energy as

$$E = \int \big(\alpha(s) E_{\mathrm{cont}}(s) + \beta(s) E_{\mathrm{curv}}(s) + \gamma(s) E_{\mathrm{img}}(s) \big)\, ds \quad (1)$$

where s denotes the arc-length along the snake (for more on the general formulation of the energies, see [20]). The details of implementation, including justification of the choice of coefficients α, β, and γ, are provided in the next section.

B. The Specifics of Grid Tracking

The grid used in the experiments consists of a set of intersecting lines. The grid has a lower image intensity than the background. Each grid line is tracked by a separate snake. There is a total of seven lines in each of two directions. The number of control points in each snake is usually set to 80. It is constant because the distance from the camera to the object is approximately the same every time, and it is desirable to maximize the size of the grid within a 640×480 image so that the lines are further apart from each other on the intensity image for more reliable detection, and to attain a sufficient number of control points per snake. Since comparisons are to be made with respect to normal tissue, the grid should bound an area such that both normal and abnormal tissues are encompassed. Point spacing within a snake and interline spacing are calculated automatically using points defined during the initial placement. It reduces interaction with the program to a minimum.

Following the grid on the skin in the experiments is unlike more common snake implementations such as a snake for tracking spatial modulation of magnetization (SPAMM) grids in cardiac MR images [20] for the following reasons.

1) Lines are placed in a nonuniform way because of perspective projection of a 3-D scene. It cannot be determined in advance how close or far they will be. As a matter of fact, some grid lines are several times closer to each other than the others in the same image.

2) Displacements are large and also nonuniform. The magnitude of displacements exceeds grid spacing, so there is a possibility of matching to the wrong snake line if not properly initialized. Initialization in the second image (after the motion) based on the location in the first image is impossible.
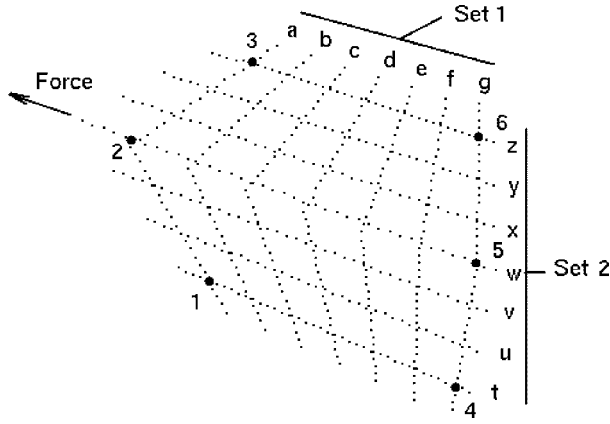
Fig. 2. Snake placement.

3) Stretching changes the shape of initially straight lines. Hence, the shape of the grid lines in the image after stretching should be approximated with curves, or at least with more than one line segment.
4) The angle between two sets of lines is not 90 degrees; it varies depending on the position of the arm (forearm).

The set of snakes is initialized in the following manner. There are two sets of intersecting grid lines to track. Stretching usually affects one set (Set One) more than the other (Set Two). This is ensured by the direction in which the skin is pulled; always along the direction of one set of grid lines. A total of six points (selected by the user) are needed to identify the region where initial placement should occur: four corner points and two more points to better approximate lines from Set One (as shown in Fig. 2). The initial snake lines are placed at equal distances within the edges of the hexagon formed by connecting these six points.

The snaxels (the snake control points) within the lines from the second set are placed at increments defined by

$$\Delta x = (x_n - x_1)r_1/n, \quad \Delta y = (y_n - y_1)r_1/n \quad (2)$$

where (x_1, y_1) and (x_n, y_n) are the two initial "end points" of the line, n is the number of control points on the line and r_1 is the ratio (normally between 1.1 and 1.2) to compensate for lines stretching past the "end points." This factor has been found to provide reliable connectedness between lines; otherwise, their intersections are lost and some correspondences cannot be found.

The control points on the lines are, thus, calculated using the following:

$$x_i = x_1 + (\Delta x)(i - n/r_2) \quad y_i = y_1 + (\Delta y)(i - n/r_2) \quad (3)$$

where i is the index of the control point, and $r_2 = 2/(r_1 - 1)$. Like r_1, the ratio n/r_2 assures that the boundary lines intersect.

Lines from the first set (undergoing the biggest deformation by virtue of the force perpendicular to them) are modeled using two segments. The number of control points in the first segment, n_{s_1}, with end points x_1 and x_{n_1}, is determined using the ratio of its length, l_{s_1}, over the entire length of the snake,

$l_{s_1} + l_{s_2}$, multiplied by the total number of points in the snake

$$n_{s_1} = (l_{s_1}/(l_{s_1} + l_{s_2}))n$$
$$l_{s_1} = \sqrt{(x_{n_1} - x_1)^2 + (y_{n_1} - y_1)^2}$$
$$l_{s_2} = \sqrt{(x_n - x_{n_1})^2 + (y_n - y_{n_1})^2}$$
$$\Delta x_{s_1} = (x_{n_1} - x_1)r_1/n_{s_1}$$
$$\Delta y_{s_1} = (y_{n_1} - y_1)r_1/n_{s_1}$$
$$x_i = x_1 + (i - n_{s_1}/(0.5r_2))(\Delta x)$$
$$y_i = y_1 + (i - n_{s_1}/(0.5r_2))(\Delta y). \quad (4)$$

The second segment with end points x_{n_1} and x_n is calculated in a similar way

$$\Delta x_{s_2} = \frac{(x_n - x_{n_1})r_1}{n - n_{s_1}} \qquad \Delta y_{s_2} = \frac{(y_n - y_{n_1})r_1}{n - n_{s_1}}$$
$$x_{n_1} = x_{n_{s_1} - 1} \qquad y_{n_1} = y_{n_{s_1} - 1}$$
$$x_i = x_{n_1} + (i - n_{s_1})(\Delta x) \quad y_i = y_{n_1} + (i - n_{s_1})(\Delta y). \quad (5)$$

The initialization is necessary for each time frame since the motion is relatively large and it is impossible to know in advance how and where the points move during the stretching.

During the fitting stage, each snake iteratively minimizes its energy to track the exact contour of the corresponding grid line. Following Williams and Shah [47], the snaxel points are moved greedily, shifting each to a new location in its neighborhood where the total energy is a minimum.

The choice of coefficients α, β, and γ in (1) is relatively simple for images before the motion. Since deformation of the grid is minimal and caused only by a natural shape and position of the arm, setting them to the same value is an effective solution. However, in order to allow the snake to follow much larger deformation caused by stretching, α and β are chosen at 0.65–0.75γ and 0.5γ, accordingly (in our setup $\gamma = 2$).

When the algorithm terminates, the entire set of snakes should lie on the grid. The last step is computing the intersection points in the images before and after the motion and calculating their 3-D displacements using corresponding range data. The grid intersection points are computed as the intersection points of the corresponding snakes. These points and their displacements are automatically fed into the FEM model, and provide the foundation for the calculation of motion and deformation parameters. Finite element modeling and its use in the proposed method are described next.

III. NONLINEAR FINITE ELEMENT MODELING OF SKIN STRETCHING

A. General Approach

The displacements of grid points are examined as reactions to the external forces applied to this object. From these observed differences in displacements, relative material properties are estimated. This approach is an adaptation of the general *inverse problem* category used in nondestructive (electromagnetic, acoustic) testing [48]. Based on the result, an attempt is made to deduce the nature of the effect that caused

the result by estimating the material properties. The general inverse problem is not solved for the trivial engineering mechanics applications. However, if the material properties are known, the surface movement can be accurately characterized. It becomes a difficult task since the material properties of skin are not well-established. Nonetheless, this method does not need precise properties, only a range of values to be specified in the model. As shown in this work, the physical properties of a second material embedded in a material of known properties can be estimated. Kallel and Bertrand [37] believe that, to overcome certain limitations, elastography should be considered within the framework of inverse problem solution.

The ANSYS program [49] is used for nonlinear FEM calculation. Version 5.3 was used on a SUN SPARC 10 with 32 MB of memory. There are almost 150 different element types in ANSYS, and each element has properties corresponding to the analysis type, object structure, constraints, and loads. The element types used in this work are elastic structural 3-D shells. It was determined experimentally that the shell provided the best accuracy versus execution time for skin modeling described next.

B. Skin Modeling

In the context of this work, tissue characterization refers to the assessment of pliability of skin, which includes tensile characteristics of the tissue and can be experienced by the patient as stiffness or tightness [1]. One way of conceptualizing this problem is to evaluate distortions of the skin that occur when skin is pulled or stretched. The skin is modeled as a nonrigid object undergoing motion. From a model-based estimation of the pointwise motion the properties of the underlying tissues can be validated.

Normal elastic skin allows almost unrestricted body movement. However, with scarring, skin material properties change and skin movement is restricted. This relationship between joint movement and skin pliability has been verified by Richard et al. [42]. Skin or soft tissue is a viscoelastic material, and its material property is a combination of elastic solids and viscous liquids. Mechanical behavior of the skin is effected mainly by three of its components: the elastin fibers network (20%), the collagen fibers (72%), and the ground substance (4%) [35]. The mechanical properties of the collagen fibers and elastin network are nonlinear, and the ground substance contributes to the viscosity of the tissues. Thus, the typical stress-strain relationship for skin is nonlinear. The behavior at low strains is controlled by the elastin network, and the collagen fibers dominate the behavior at high strains. The procedure of scar healing is accompanied by the deposition of thick bands of collagen with no overall orientation pattern. As a result, whirl-like patterns are observed, as opposed to parallel patterns found in normal skin. This process changes the mechanical properties of the skin and its deformation with respect to various stresses.

C. Theory of Elasticity and Stress-Strain Equations

The theory of elasticity (for more on elasticity and FEM, see [50]) shows that the response of a solid body to external forces is influenced by the geometric configuration of the body as well as the mechanical properties of the material. Elastic materials are materials in which the deformation and stress disappear with the removal of external forces. This is true for the presented in vivo experimental setup (for the produced range of displacements); therefore, elastic formulation is applicable.

The stress p in the element $\triangle A$ of area is defined as the average force per unit area when the area $\triangle A$ approaches zero, or

$$p = \lim_{\triangle A \to 0} \frac{\triangle F}{\triangle A} = \frac{dF}{dA}. \tag{6}$$

The stress vector depends on the location of the point as well as the orientation of the surface through the point. Let σ represent the normal stress, i.e., the component of stress *perpendicular* to the plane in which it acts. The shear stress is the component of stress which lies *in* the plane and is denoted by the symbol τ. Thus

$$p^2 = \sigma^2 + \tau^2. \tag{7}$$

The strain, ϵ, is defined as the change in displacement, u, with the change in length, x, or

$$\epsilon = \frac{\partial u}{\partial x}. \tag{8}$$

The modulus of elasticity, or Young's modulus E can be defined as

$$E = \frac{\Delta \sigma}{\Delta \epsilon} \tag{9}$$

where $\Delta \sigma$ is the stress change and $\Delta \epsilon$ is the strain change. The stress σ can be viewed as force per unit area and the strain ϵ as changes of lengths per unit length.

The Poisson's ratio ν is defined as the ratio of the magnitude of the transverse strain to the magnitude of the axial strain. In other words, consider a parallelepiped element under a uniaxial stress σ_x. When there is an elongation in the x direction, there will be contractions in the y and z directions. These are given by

$$\epsilon_y = \epsilon_z = -\nu(\sigma_x/E). \tag{10}$$

For a general state of stress, the stress-strain relations, which are known as "generalized Hooke's law," consist of the equations

$$\epsilon_x = \frac{1}{E}[\sigma_x - \nu(\sigma_z + \sigma_y)], \qquad \lambda_{xy} = \frac{1}{G}\tau_{xy}$$
$$\epsilon_y = \frac{1}{E}[\sigma_y - \nu(\sigma_x + \sigma_z)], \qquad \lambda_{yz} = \frac{1}{G}\tau_{yz}$$
$$\epsilon_z = \frac{1}{E}[\sigma_z - \nu(\sigma_x + \sigma_y)], \qquad \lambda_{zx} = \frac{1}{G}\tau_{zx} \tag{11}$$

where λ_{xy} is a shear strain component of a shear stress component τ_{xy} and G is called the modulus of elasticity in shear, or the modulus of rigidity

$$G = \frac{E}{2(1+\nu)}. \tag{12}$$

These relations complete the system of field equations necessary to formulate a problem in elasticity.

General *nonlinear* deformation theory defines the displacement field as a combination of rigid-body motions and pure deformations [50]. Rigid-body motions include translations and rotations. Their main property is that the distance between any pair of material points remains unchanged. Any quantity that measures the *change* in length between the neighboring points is a measure of pure deformation.

D. Large-Strain Nonlinearities in FEM

Static nonlinear FEM problem [50] can be expressed as

$$[K(\bar{u})]\bar{u} = F(\bar{u}) \tag{13}$$

where both a matrix of stiffness coefficients $[K(\bar{u})]$ and a force vector $\bar{F}(\bar{u})$ depend on the displacement vector $\bar{u}$. Nonlinear analysis must be considered if large displacements occur with linear materials (*geometric nonlinearity*), small displacements occur with nonlinear stress-strain relationships for structural materials (*material nonlinearity*), or a combination of both effects. The first is the one predominantly used in this work. The type of geometric nonlinearities accounted for is *large strain* that assumes that the strains are no longer infinitesimal (they are finite). Shape changes and rotations are also taken into consideration. The applied loads on a body make it move (or deform) from the position $\bar{u}_1$ to the position $\bar{u}_2$. Hence, the displacement vector is

$$\bar{u} = \bar{u}_2 - \bar{u}_1. \tag{14}$$

The deformation gradient can be defined as

$$[G] = \frac{\partial \bar{u}_2}{\partial \bar{u}_1} \tag{15}$$

where the deformation gradient includes the volume change, the rotation, and the shape change. The volume change at a point is

$$\frac{dV_2}{dV_1} = \det[G] \tag{16}$$

where $\det$ denotes determinant of the matrix. The deformation gradient can be separated into a rotation and a shape change using the right polar decomposition theorem

$$[G] = [R][U_s] \tag{17}$$

where $[R]$ is the rotation matrix and $[U_s]$ is the right stretch (shape change) matrix. Once a stretch matrix is known, a logarithmic or Hencky strain measure in tensor (matrix) form is defined as

$$[\epsilon] = \ln[U_s] \tag{18}$$

or, equivalently, through the spectral decomposition of $[U_s]$

$$[\epsilon] = \sum_{i=1}^{3} \ln(\lambda_i) e_i e_i^T \tag{19}$$

where λ_i are eigenvalues of $[U_s]$ (principal stretches) and e_i are eigenvectors of $[U_s]$ (principal directions). Hence, from (17) we can calculate the average rotation at a point. Computationally, incremental approximation is used [49] and

increment of the deformation gradient at the current time step n is defined using the previous time step $n - 1$

$$[\Delta G_n] = [G_n][G_{n-1}]^{-1}. \tag{20}$$

IV. BURN SCAR ASSESSMENT TECHNIQUE

A. Detection of Burn Scars

The next step is to find the location of the scar, if one exists in the image. Since the loading in the presented experiments does not induce strains above the breaking point of skin, a material model that captures only the normal skin response to stretching is appropriate. To be effective, the solution requires an energy-based material model, hyperelastic shell elements and large strain integration and analysis.

In these experiments the model is *local*. Only the part of the forearm (or arm) with the grid painted on the skin is considered. The grid tracking described in Section II-B provides the necessary information about the keypoints (points used to build a model's geometry) and the displacements. Coordinates of these points are converted into 3-D coordinates using range information. Keypoint information goes directly into a FEM model. The program generates areas of the model that approximate forearm (arm) geometry. The meshing of these areas results in a more dense number of nodes (361) than the number of grid points/keypoints (49). Similarly, from the images after the motion, model displacements (base nodal displacements to be used during the later stages) are computed. The rest of the model, i.e., initial material properties and number of areas, is case-independent.

The procedure for generating a mesh of nodes and elements consists of three steps: 1) set the element attributes, 2) set meshing controls, and 3) generate the mesh. In these experiments the mesh is *mapped*. This means that it is restricted in terms of the element shape it contains and the pattern of the mesh. The mesh contains only quadrilateral elements (a total of 324 elements and 361 nodes). In addition, it has a regular pattern, with obvious rows (or columns) of elements. This is achieved based on the regularity of the grid's geometry recovered with snakes from the range data. This also allows other experiment-independent meshing controls; for example, the element sizing is the same. It was chosen experimentally as a tradeoff between desired accuracy and execution time. Such a setup allows for automatic finite element model generation without human intervention, which is necessary for the large-scale clinical testing.

One way to locate the abnormality is to compute the total mechanical strain level throughout the skin surface. Nine levels of strain are defined. Normal skin usually has relatively even distribution (an absence of the lowest strain level) in the middle of the area of observation. Abrupt variations (changes of at least 40% to the lowest strain level occurring within a single model area) in the skin strain levels indicate the existence of the area with the different material properties. Areas with the lowest strain normally coincide with the true location of the abnormalities. The only notable exceptions are images with smaller displacements where the force (and, of course, reaction to the force) is not propagated all the way to

the opposite boundaries. As a result, some very small areas of low strain are allowed along the boundaries for normal skin areas in such cases. Hence, skin regions with low strains other than the boundary are ruled as being predominantly abnormal.

Kallel and Bertrand [37] described the stress field of compressed soft tissue as high near the boundaries of the compressor and decreasing with distance from these boundaries. In our experiments, the effect is exactly opposite to their stress decay: both stress and strain are the lowest near the boundaries of the grid (except for the boundary where the force is applied), unless the abnormality is detected inside the area. This is because our setup involves tensile loading, and Kallel and Bertrand studied compressive loading.

B. New Method for Recovering Material Properties of Scars

The method for recovery of unknown material properties is based on the following observation. If displacements of the boundary points only are applied and the value of unknown elasticity is varied, the resulting displacements of the nodes of the FEM model change also. If there were correct elastic properties for both areas, then the displacements of all of the object's points would have been equal to the motion between two time frames calculated using the available range data. Hence, new nodal displacements can be compared with the base displacements (defined in Section IV-A), and the difference that would guide the search to the correct value of Young's modulus can be estimated. True displacements are known not only for the keypoints as a result of the snake fitting procedure to the grids on the images before and after the motion, but also for all of the nodes as a result of the inverse FEM computation. Since density of the nodes is greater than density of the keypoints, it allows better error estimation precision at the expense of higher computational complexity. This increase in execution time can, of course, be neglected for models like this one with a relatively small ratio between nodes and keypoints. Some important properties of the initial model affected by this step should be reiterated. The preliminary model incorporates displacements of all keypoints as both loads and boundary conditions. Positions of grid boundary points after the motion recovered by active contours specify not only reactions to external forces, but also boundary conditions necessary for the model. However, all subsequent FEM computations use a somewhat different model that ignores displacements of interior points of the grid. This way, correct elasticity is a cause of correct displacements of such points (by participating in the faithful propagation of boundary displacements). Another important outcome of the first step is localization of abnormal (less elastic) area(s). It usually coincides with the lowest strain on the surface of the object. The lowest strain is determined by using nine levels of strain throughout the surface of the model and choosing the first one. This area(s) is the place where material properties that contribute to the total error are gradually change.

The error is computed by comparing true displacements of the nodes (or keypoints) after the motion with a change in their positions predicted by the FEM model incorporating a
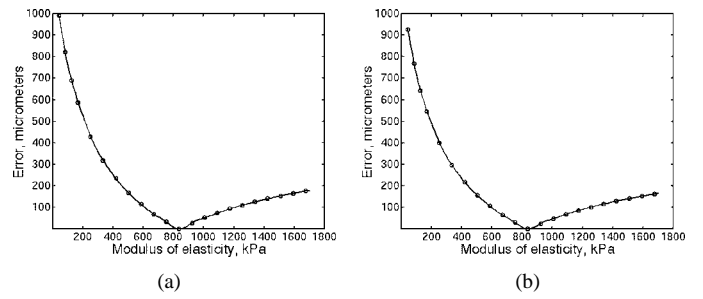

Fig. 3. Approximations of the error function using (a) 361 FEM nodes and (b) 49 FEM keypoints.

current hypothesis about Young's modulus of the burn scar. The error is defined per node or keypoint.

Fig. 3 shows a set of error functions derived experimentally [51] as a result of investigating properties (by applying the described algorithm) of elastic materials, scaled per node/keypoint. Circles are computed function values and lines denote results of interpolation. Fig. 3(a)–(b) explains that the correctness of the result is not affected by using 361 nodes [Fig. 3(a)] or 49 keypoints [Fig. 3(b)]. For the remainder of this paper, nodes are used in all other error graphs because of their higher density.

For the different steps of the method to be successful the analysis of displacement thresholds is as follows. First, as mentioned, the displacements should be sufficient to detect abnormal areas (threshold $T_1 = 0.5$ cm). Second, after adjusting for the global translation, maximum displacement should be large enough to apply an iterative descent search, ideally more than 1 cm (threshold T_2). However, even 0.8 cm displacement is adequate for achieving acceptable results. This condition is "responsible" for most of the first part of the curve where the function is decreasing (Fig. 3). It allows one to get very close (within 2%) to the minimum. And the last, but certainly not least, threshold (T_3) monitors maximum stretching in the newly detected burn scar. It accounts for the second part of the curve where the function is increasing and is necessary for the precision of the result and fast success of an iterative descent method. Kallel and Bertrand [37] also noted that displacement noise reduces the quality of the reconstruction of low-contrast areas. This statement is generalized as displacement thresholds that estimate signal-to-noise ratio (SNR) for a given application.

Because of the observed similarities in error functions for various elastic materials, error minimization can be applied. A search applicable to this task is Brent's method in one dimension [52], which attempts to utilize parabolic interpolation. To be acceptable, the parabolic step must fall within the bounding interval (x_1, x_2) and imply a movement from the best current value that is less than half the movement of the step before the last (to insure convergence). The step *before* the last is chosen to allow the algorithm one bad step. This can be useful to get the search out of the local extremum. The distance from a point already evaluated to a new point is proportionally limited by the tolerance, which can be varied. Usually, sufficiently smooth functions are parabolic near the minimum. Hence, the parabola fitted through any three points will find a point close

to the minimum in a single step. Since finding an abscissa rather than an ordinate is desired, the procedure is called *inverse parabolic interpolation*. The formula for the abscissa x that is the minimum of a parabola through three points $f(a)$, $f(b)$, and $f(c)$ is

$$x = b - \frac{1}{2} \frac{(b-a)^2[f(b)-f(c)] - (b-c)^2[f(b)-f(a)]}{(b-a)[f(b)-f(c)] - (b-c)[f(b)-f(a)]}.$$
(21)

The formula fails only if the denominator is zero. This would mean that all three points are collinear and minimum of the parabola is infinitely far away. A case like this is impossible in this problem domain as long as correct bounding interval is selected. The analysis of function behavior during the experiments in Section IV-B will explain this. In the worst possible case, where parabolic steps do not approach the solution, the method still succeeds by employing the golden section search. Hence, depending on the behavior of the function, the method alternates between these two methods.

Error minimization utilizing the iterative descent method takes place in the neighborhood of the known elasticity. This neighborhood can be defined exactly based on the known properties of the first material and the predicted behavior of the second. Minimum of the error function corresponds to the correct elasticity of the second material. Hence, the solution is completely based on the comparison of the nodal displacements obtained by modification of Young's modulus of the abnormal area (second material) with the base displacements. To summarize, true displacements are recovered for the keypoints from the images (before and after the motion) using snakes, and then for all nodes using our FEM model. A similar procedure can be followed using level of strain as a guidance instead of displacements. However, it was found that displacement analysis is more precise for burn scar data (Section V). Fig. 4 shows steps of the proposed method.

V. BURN SCAR EXPERIMENTS

A. Sources of Errors

Before presenting the results, the potential sources of input errors must be investigated. A range scanner is a device that measures the distance of points in a scene from itself and can provide a 3-D representation of the objects. A structured light K2T scanner made by K2T Inc. (Duquesne, PA) is used for this research. It consists of a projector that contains a multistripe liquid crystal shutter under computer control. This is used to project a sequence of horizontal stripe patterns into the scene. Intensity images are captured with a camera. The stripe sequence visible at each pixel identifies the location of the visible surface point. The following problems are some of those one has to face with a similar range scanning technique.

1) Depth at some pixels cannot be correctly estimated due to occlusion, noise, etc.
2) Accuracy of the system itself is limited. It is a function of the size of the voxels formed by the intersection of the projection of the stripes with the backprojection of
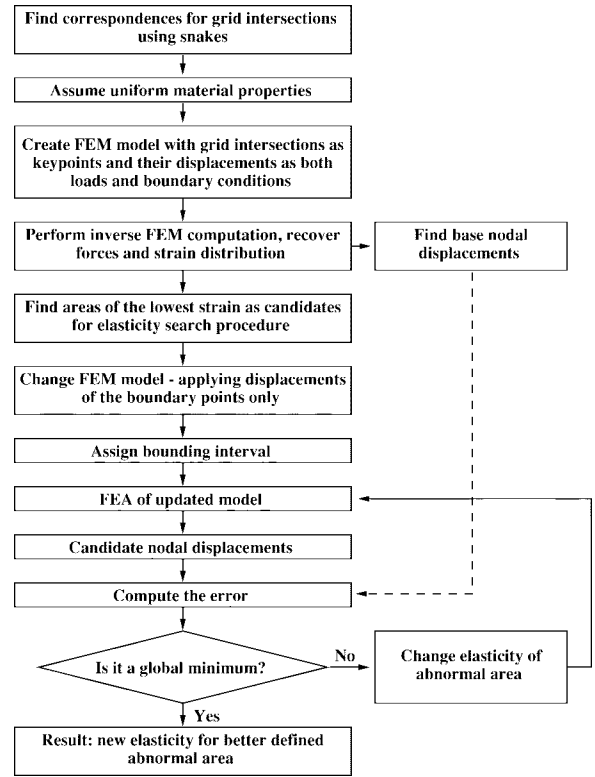

Fig. 4. Algorithm of the new method.

the camera pixels [53]

$$A = \frac{1}{2} V_b^{1/3}$$
(22)

where A is the system's accuracy and V_b is the volume of bounding box enclosing voxel. It has been found experimentally that the scanning error lies within the interval from 0.5 mm to 1 mm. The error matters in the context of displacements that are usually between 8 and 16 mm. Therefore, the error constitutes about 6% of displacement values on average. Results are affected when error is greater than 20% of displacements.

3) Accuracy of locating the grid points using snakes is another source of the error. This error is relatively small (1–2 pixels); however, it adds to the former error and together they define an upper bounds on accuracy of the results. In practice, it prevents optimal precision in localization of the feature points and the stress-strain areas. However, the obtained precision was adequate for burn scars. The results were validated by the judgments of physicians.

B. Representative Cases

The method was applied to the images of scars of patients from the Tampa General Hospital Burn Unit. Currently, the selection of patients is limited to those with scars on arms or forearms since they are easier to deal with, considering the specifics of the range camera used.

Let us consider three cases of different complexity. The first case introduces a relatively easy to observe scar on the arm with conspicuous boundaries. Fig. 5(a) and (b) shows the gray
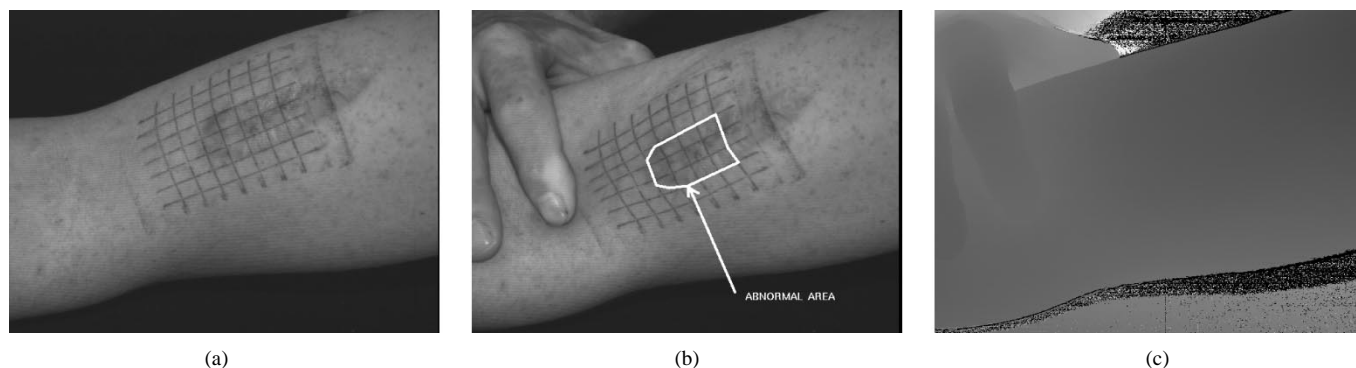
(a)   (b)   (c)

Fig. 5.   (a) and (b) Intensity images of the skin with the grid. (c) The range image of the skin after stretching.

(a)   (b)   (c)

(d)   (e)   (f)
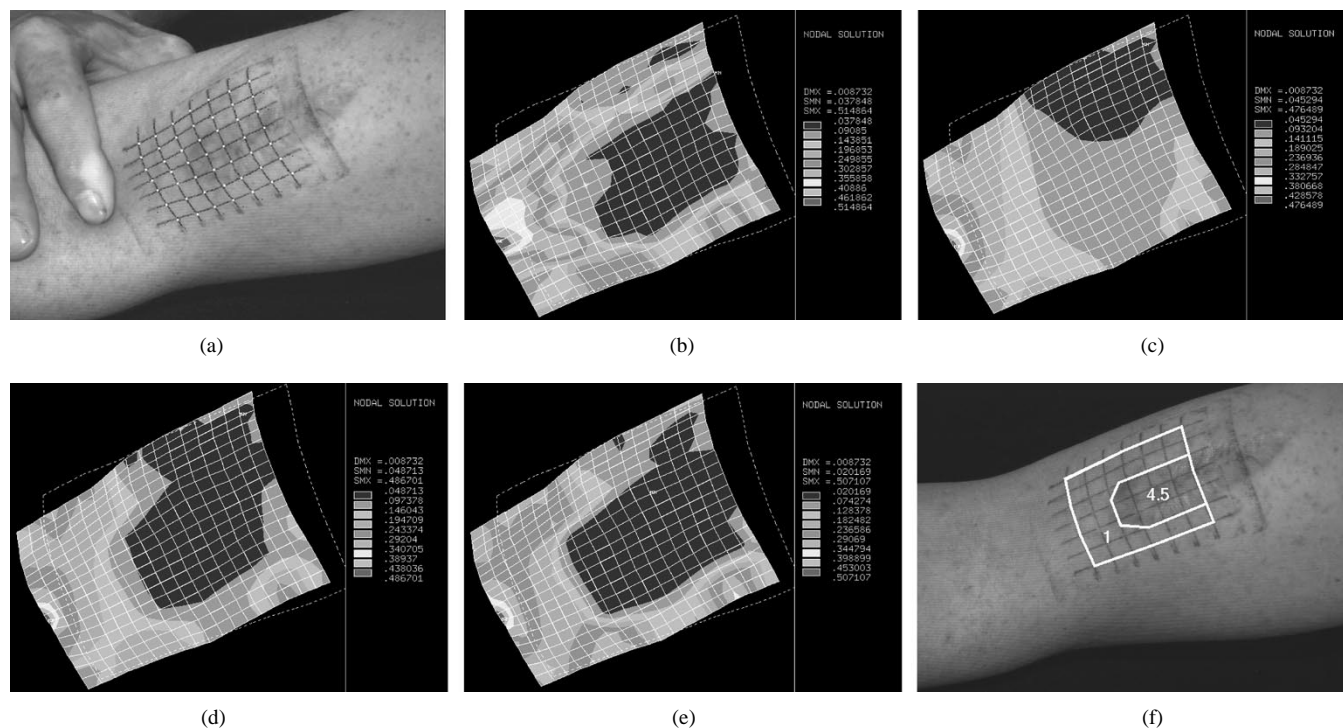
Fig. 6.   (a) Tracking the grid with snakes. (b)–(e) Progress of the method (data for the first patient). Nine levels of strain are displayed in the grid area from the lowest (blue) to highest (red). (f) Scar rating by the specialist.

level intensity images of the ventral side of the patient's arm with the burn scar before and after stretching, respectively. The range image corresponding to Fig. 5(b) is shown in Fig. 5(c). It is apparent that the displacements are sufficient for the algorithm to come upon the scar area. The forces necessary to produce the desired range of displacements are within the comfort range for the patients. Increased stretching force improves the accuracy of the method. Of course, no pain or even discomfort should ever be inflicted upon the patient (as a matter of fact, they are usually offered to stretch the skin themselves),[1] and, therefore, the forces are limited.

Snakes successfully detect the grid points and help in establishing feature point correspondences between the frames [Fig. 6(a)]. The finite element model is generated automatically using grid intersections to create keypoints and correspondences to find displacements. Four keypoints define an

[1] All patients participated in the project after signing an informed consent form.

area which is then split up into elements using elastic shell type of the element with a thickness equal to the average thickness of normal skin (0.0012 m [54]). The latter is a summation of thicknesses of its layers. These layers are the Epidermis (or outer layer), the Dermis and the Subcutaneous layer (or lower dermis). Material properties are selected based on the analysis of the following. Many researchers ([55]–[57]) have used Poisson's ratio as 0.49 based on the assumption that soft tissue is nearly incompressible. There is less agreement on Young's modulus, but careful comparison allows us to select a certain range of elasticity (from 10 to 100 kPa) that contains values most authors ([55], [56], [58]–[61]) incorporated into their models. These ranges are sufficient for our goal—distinguishing between normal tissue and burn scars.

Despite the nonlinear nature of the problem, the solution takes, on average, less than one minute because of the relatively small number of elements. The displacements of the
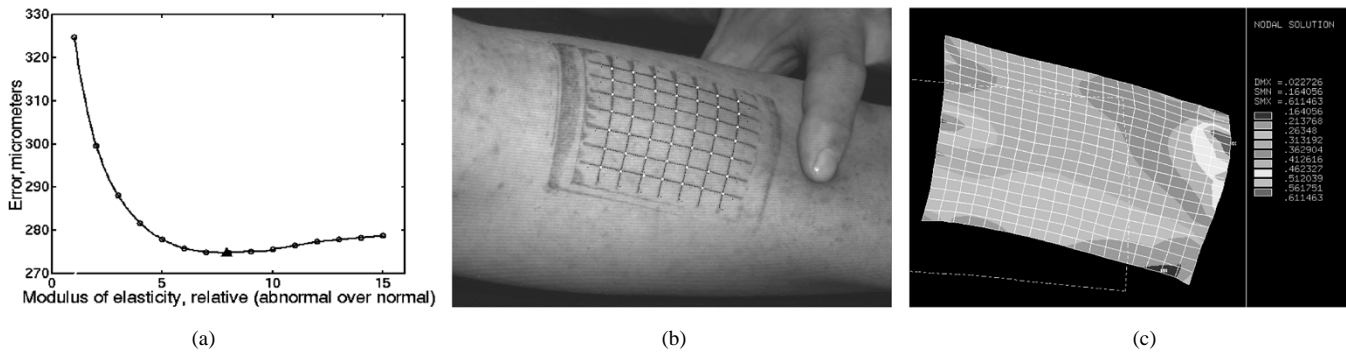
Fig. 7. (a) Error function (defined per node). (b)–(c) Detection process and results of the method for the other arm (without burn scars) of the same patient. Nine levels of strain are displayed from the lowest (blue) to highest (red). The lowest strain is not present in the middle of the area.

skin in the grid area are adequate for the success of the first step. Such displacements allow the identification of low strain areas of the model that are candidates for an iterative descent algorithm [Fig. 6(b)]. The legend column on the right of the strain distribution shows (top to bottom) maximum displacement (m), and minimum and maximum strain. Nine levels of strain are displayed in the grid area, from the lowest (blue) to highest (red). In this case, 12 out of 36 grid areas approximate the burn scar shape.

The procedure developed in Section IV-B is fully applicable here. However, from now on, when we discuss elasticity of a burn scar, we will use relative rather then absolute values. Relative means defining properties of an abnormal area as multiples of normal skin properties. Since there exists a range of properties for normal human skin rather than exact properties for this particular patient, this is a better estimate. In engineering mechanics there exists a simple setup when one end of the material sample is fixed while variable weights are applied to the other end. Length of the stretchable part is measured with a micrometer before and after the stretching to determine change in length and, consequently, strain as well as modulus of elasticity. This setup is applied to find modulus of elasticity for different elastic materials (elastic bandages) and then compared it to the results achieved with this new method. The difference was less then 0.12% in all experiments. However, it is not feasible to do such testing for humans. Having absolute estimates is not possible at this time because some external references cannot be obtained precisely (for example, skin and burn scar thickness for each patient). And it does not appear to be necessary because, to determine the success of treatment, change in elastic properties of skin must be determined, and relative values are sufficient for such a procedure. Also, because of this approach, it is not necessary to know the value of the force applied as opposed to the work by Kallel and Bertrand [37].

Applying Brent's method (again, the error is computed by comparing internal nodal displacements to grid motion) allows not only finding Young's modulus of the burn scar, but also making the scar area much more perceptible in terms of strain analysis. Fig. 6(c)–(e) shows the starting point of the method, one of intermediate results and the final result. Now the burn scar is clearly outlined. The relative elasticity of the scar is estimated at 7.9 (790%).

Location of abnormalities and their elasticity is validated using the ratings by the plastic surgeons from Tampa General Hospital Burn Unit on the scale from one to five as follows:

1) normal *for the person* and location;
2) minimal decrease in pliability/elasticity/intrascar movement;
3) moderate decrease;
4) large decrease;
5) extreme decrease (no intrascar movement).

Physicians rate the scar with respect to the normal skin of the patient so that the ratings are compatible to our concept of *relative* elasticity. For this patient, the burn scar was rated as 4.5 [Fig. 6(f)]. Ratings are compared in Section VI. The match in scar localization comparing to results of this experiment is obvious [see Fig. 6(e)–(f)].

Another (rather mathematical) proof of the result is investigation of the function behavior within the bounding interval. The function [Fig. 7(a)] is very similar to one found for elastic materials (Fig. 3). It has only one global minimum and no local minimums. However, the nodal displacement error *never* decreases below $250.705 \ (10^{-6})$ m. The explanation includes both noise in the displacements' estimates (relatively small, does not exceed one-quarter of 1 mm per node) and the complexity of the motion (the model captures only stretchy response). Still, the precision is adequate, and the burn scar is clearly defined.

For the sake of comparison, the same place on the other arm of the same patient that does not contain any abnormalities (Fig. 1) is considered. Fig. 7(b)–(c) shows detection results on the intensity image after stretching and results of the first step (detection of possible abnormality), respectively. Strain distribution in the middle of the area is relatively even. Since it is normal and uniform, the process concludes without a burn scar being detected.

In the second case, Fig. 8(a) and (b) shows the gray level intensity images of another patient's skin before and after stretching, respectively. The range image corresponding to Fig. 8(b) is shown in Fig. 8(c). This case is much more complicated. First, this patient's arms do not have any patches of "normal" skin, only burn scars of different degree. Still, the algorithm can handle this because the physicians in this case are interested in the relative difference in elasticity between more abnormal and less abnormal (instead of between

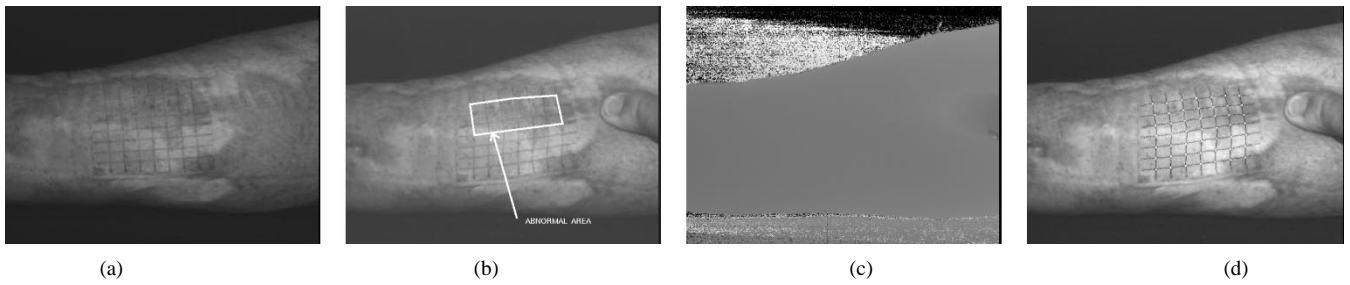|			
(a)	(b)	(c)	(d)

Fig. 8.   (a) and (b) Intensity images of the skin with the grid (for the second case). The abnormal area was outlined by the physician. (c) The range image of the skin after stretching. (d) Detecting the grid after stretching.
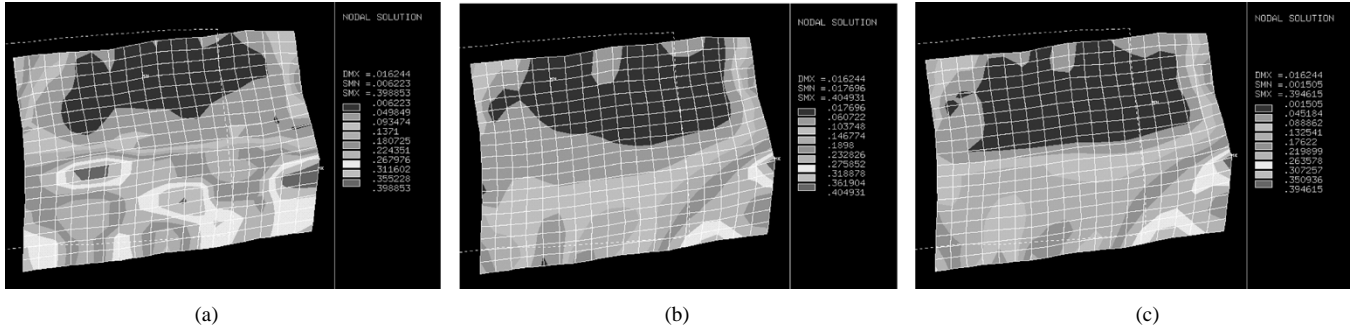

(a)	(b)	(c)

Fig. 9.   (a) and (b) Iterations and (c) results of the method (strain distributions).

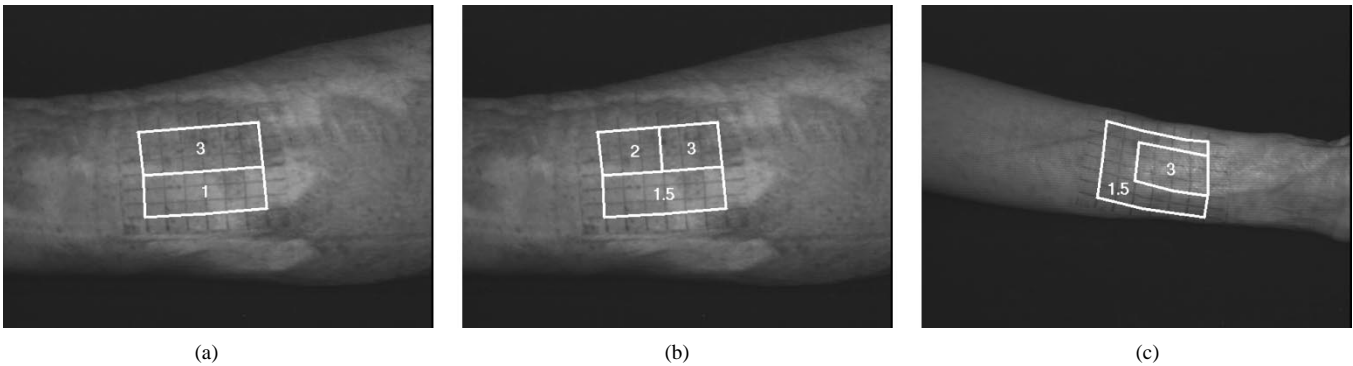|		
(a)	(b)	(c)

Fig. 10.   (a) and (b) Rating of the scar for the second patient by two physicians. (c) Rating by the specialist for the third patient.

abnormal and normal) skin. Despite the changes in intensity in the image, the grid detection part is still robust [Fig. 8(d)].

This allows the localization of abnormal areas [Fig. 9(a)]. Iterative descent is applied again (the starting point is shown in Fig. 9(b)]; however, there is a slight problem: neither of the images in the created set passes the third threshold test described in Section IV-B. The explanation is simple: since there is no normal skin, large displacements within "more abnormal" are virtually impossible. Most of the displacements within this area is below 2 mm as opposed to around 4 mm in the previous case. Since there is no increasing part of the function, when should the procedure stop to avoid unnecessary computation? At every step, the rate of error decrease per change in modulus of elasticity was evaluated. It starts out at 9.40% and continues at a reducing rate. An empirically determined threshold of about 2% is the required stopping condition. Relative elasticity of "more abnormal" area is 5.1 [Fig. 9(c)]. Since the second part of the curve does not seem to be very reliable, only the first part is plotted [Fig. 12(a)].

To differentiate an influence of the third threshold as opposed to the effect of noise, the experiment was repeated with other images of the same scar for the same patient. Both the decrease in error and the resulting elasticity were the same. For the second patient, the "more abnormal" area was rated by the specialists as three [Fig. 10(a) and (b)]. Again, it is moderate *relatively* to the surrounding tissue.

Another interesting case represents a class of burn scars that do not appear to be very different from surrounding tissues. Fig. 11(a) shows the gray level intensity image of the patient's skin after stretching with the scar's outline. The first step of the method works well in pointing out the presence of the scar [Fig. 11(b)]. However, detection of the scar true boundaries is next to impossible at this stage of the algorithm and will be determined during the last step (Fig. 4). Images for this patient pass all threshold conditions that permit precise computation of scar elasticity. The resulting relative elasticity of the burn scar is 3.2 [Fig. 11(c)]. The physician's rating for this patient is 4 for our target area and 3.5 for surrounding areas [Fig. 10(c)].
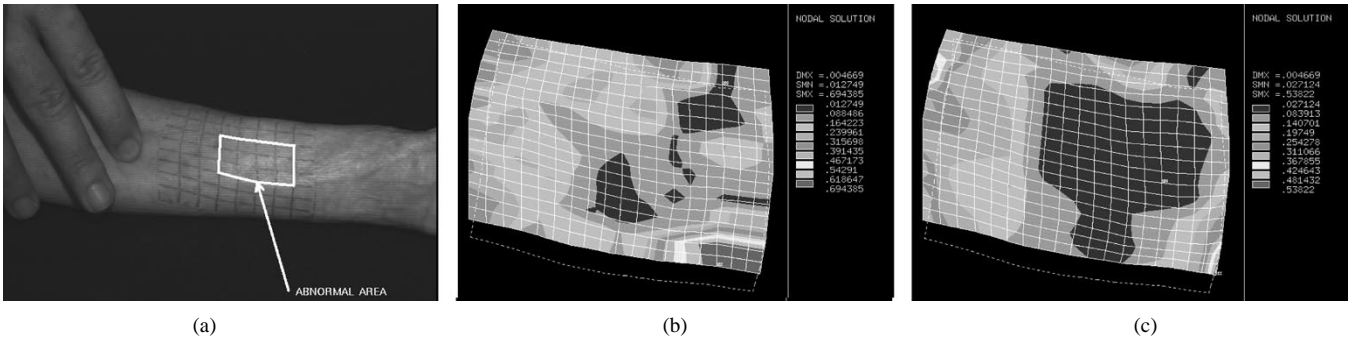
Fig. 11. (a) Intensity image of the skin with the grid (for the third patient). (b) Result (strain distribution) of the first step of the method (initial detection of the burn scar). (c) Result with recovered elasticity.
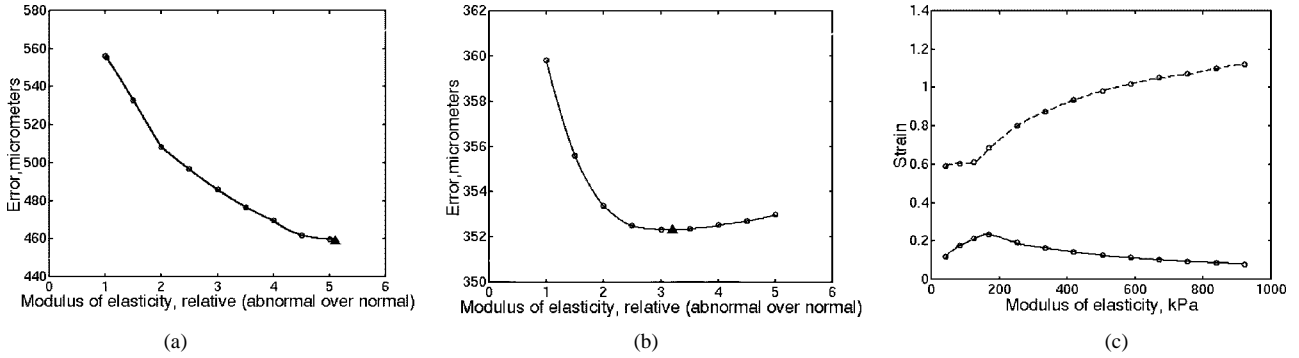

Fig. 12. (a) Error function for the second patient. (b) Error function for the third case. (c) Minimum and maximum strain functions. The difference between them becomes greater as we increase Young's modulus of the abnormal area.

Error function is well-behaved for this patient, which explains the success of the minimization procedure [Fig. 12(b)].

C. Discussion

It is interesting to compare results received in the first two cases. The source for possible confusion is the statement that 7.9 in the first case seems worse that 5.1 in the second. At first, it appears contrary to the observations, which suggests presence of greater abnormalities in the second example. Explanation lies again in the relative nature of the rating scale. For the first patient who has only a small abnormal area, the difference is greater than for the second, who has almost no normal tissue. The normal/abnormal ratio is certainly greater in the first case, although the level of abnormality is not as drastic.

If the modulus of elasticity of normal skin within the defined range is changed, the resulting absolute elasticity of burn scar changes as well (proportionally). Still, the strain table remains the same, and, even more importantly, so does relative elasticity of the scar.

Hence, the method makes it possible to introduce a set of standard measurements sufficient for individual burn scar assessment. Moreover, even the first step of the method can tell burn scars from normal skin, not only for individual patients, but also across the patients. The method can be used across patients by comparing differences in displacements in normal versus abnormal tissue, if these tissues are rated at least 0.5 level apart from each other. This can be explained with a following experiment: as Young's modulus of the abnormal

area increases, the gap between it and the rest widens also in the quantitative sense: most of the time minimum strain is decreasing [Fig. 12(c), solid line] and maximum strain is increasing (dashed line).

VI. SUMMARY AND VALIDATION OF THE RESULTS

Table I summarizes application of the method to the data available for different patients and simulated abnormalities. All of the abnormalities (including both burn scars and simulated scars) were detected (found in the sequence in the same area as the physician), and images of normal skin were identified without false alarms.

Table II proves that the method of elasticity analysis is robust enough to be successfully applied to various categories of image sequences. T is the total number of image sequences that belong to a specific category; T_1, T_2, and T_3 are passing conditions (thresholds) that are evaluated in order to estimate if the quality of the motion, and the image data itself are

TABLE I
SUMMARY OF SCAR DETECTION FOR ALL IMAGES

Categories of images	Total	Scars Detected
All Images	36	36
Images of Normal Skin	14	0
Images with Abnormalities	22	22
Images with Simulated Abnorm.	7	7
Images with Burn Scars	15	15

100% detected (22/22); 0% false positives (0/14).

TABLE II
SUMMARY OF ELASTICITY ANALYSIS FOR ALL IMAGES
WITH BURN SCARS OR SIMULATED ABNORMALITIES

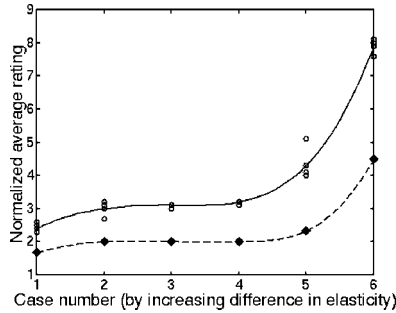| Categories of images	T	T_1	T_2	T_3
Images with Abnormalities	22	22	21	18
Images with Simulated Abnormalities	7	7	7	7
Images with Burn Scars	15	15	14	11

Fig. 13. Comparison of scar rating by the specialists (diamonds denote produced ratings, dashed line—interpolation function) with our method's results (circles denote results for different image sequences, solid line—interpolation function).

sufficient to apply certain steps of the method as described in Section IV-B. Elasticity of burn scars was recovered very precisely (except for some images of the second patient). Summarizing thresholds and conditions, the SNR change in displacements caused by differences in normal and abnormal elasticity cannot be too small over noise/inaccuracy in displacements.

In these experiments, there were two or more image sequences for each of the patients. The image sequences differ in the location and the direction of the pulling force. Despite these differences, the results for each patient were the same, regardless of the sequence chosen for the analysis as long as it conforms to the threshold requirements. However, the most important accomplishment of the method can be realized by comparing obtained results (Fig. 13, where circles denote results for different image sequences and solid line represents interpolation function) with independently produced ratings of burn scars by the specialists from Tampa General Hospital Burn Unit (diamonds denote produced ratings; dashed line: interpolation function). Both sets of results (average rating per patient) correlate for all cases of burn scars, despite the difference in scales. However, the proposed method achieves better resolution, detecting even very small differences in elasticity.

VII. CONCLUSIONS AND FUTURE RESEARCH

In this work we have presented a new method of skin motion analysis from range image sequences using iterative descent search that guides nonlinear FEM model building. This method is capable of objective detection of the differences in elasticity between normal and abnormal tissue as well as measuring relative scar elasticity and ranking the scar on the scale similar to the one used by physicians. Independence of the load magnitude within the produced range of displacements

offers the obvious benefit of avoiding the need for calibration in every experiment. The forces necessary to produce the desired range of displacements are within the comfort range for the patients. Experimental results demonstrate the success of the proposed algorithms applied to the detection of burn scars based on the evaluation of their elastic properties relative to the surrounding areas.

This method will be utilized for the quantitative assessment and comparison of burn scar treatment results. The method will allow estimation of the progress in scar healing as a function of the difference in its elastic properties as they approach elastic properties of the normal skin.

The necessary assumptions for all of the presented experiments include the knowledge of the material properties of the object and the availability of the accurate range data. The mechanical properties of the skin vary with location and direction or are anisotropic. The variation of directional components of Young's modulus to approximate anisotropic skin properties was tested. However, reduction in the total error was not very significant, which can be explained by the nature of the experimental setup based on the unidirectional stretching. Forces from different directions were applied and results were received with standard deviation of less than 10% in the initial investigation. This is the topic of ongoing research. Other directions in future work include time-dependent experiments involving evaluation and rating of results after applying various existing healing techniques.

The use of the described method in the analysis of nonrigid motion is currently being tested on a larger set of images and extended by the authors' research group to other biomedical applications like facial expression analysis, cardiac motion, and hand [14] and knee modeling. The ability to simulate human movement and accurately compute load histories is important where exposure to different load environments can alter the functional properties of bone and soft tissues.

REFERENCES

[1] P. S. Powers, "Introduction to the Tampa Bay Regional Burn Center," Univ. of South Florida, Tampa, FL, Tech. Rep., May 1994.
[2] A. A. McHugh, B. J. Fowlkes, E. I. Maevsky, D. J. Smith Jr., J. L. Rodriguez, and W. L. Garner, "Biomechanical alterations in normal skin and hypertrophic scar after thermal injury," *J. Burn Care, Rehab.*, vol. 18, pp. 104–108, Apr. 1997.
[3] D. Metaxas and D. Terzopoulos, "Constrained deformable superquadrics and nonrigid motion tracking," in *Proc. IEEE Conf. Computer Vision and Pattern Recognition*, Hawaii, 1991, pp. 337–343.
[4] M. Yamamoto, P. Boulanger, J.-A. Beraldin, M. Rioux, and J. Domey, "Direct estimation of deformable motion parameters from a range image sequence," in *Proc. IEEE 3rd Int. Conf. Computer Vision*, Osaka, Japan, Dec. 4–7, 1990, pp. 460–464.
[5] D. DeCarlo and D. Metaxas, "Adaptive shape evolution using blending," in *Proc. 5th Int. Conf. Computer Vision*, Boston, MA, June 1995, pp. 834–839.
[6] W. Neuenschwander, P. Fua, G. Szekely, and O. Kubler, "Deformable Velcro surfaces," in *Proc. 5th Int. Conf. Computer Vision*, Boston, MA, June 1995, pp. 828–833.
[7] S. Sclaroff and A. P. Pentland, "Physically based combinations of views: Representing rigid and nonrigid motion," in *Proc. 1994 IEEE Workshop on Motion of Non-Rigid and Articulated Objects*, Austin, TX, Nov. 11–12, 1994, pp. 158–164.
[8] A. Young and L. Axel, "Non-rigid wall motion using MR tagging," in *Proc. Computer Vision and Pattern Recognition*, Champaign, IL, June 1992, pp. 399–404.
[9] D. Metaxas and E. Koh, "Efficient shape representation using deformable models with locally adaptive finite elements," in *SPIE Vol.*

2031, Geometric Methods in Computer Vision II, San Diego, CA, pp. 160–171, July 1993.

[10] M. H. Davis, A. Khotanzad, D. P. Flamig, and S. E. Harms, "A physics-based coordinate transformation for 3-D image matching," *IEEE Trans. Med. Imag.*, vol. 16, pp. 317–328, June 1997.

[11] S. Basu and A. Pentland, "A three-dimensional model of human lip motions trained from video," in *IEEE Nonrigid and Articulated Motion Workshop*, San Juan, Puerto Rico, June 1997, pp. 46–53.

[12] W.-C. Huang and D. B. Goldgof, "Point correspondence recovery in nonrigid motion using nonlinear finite element modeling," in *Proc. Asain Conf. Computer Vision*, Osaka, Japan, Nov. 23–25, 1993, pp. 256–259.

[13] W.-C. Huang, D. B. Goldgof, and L. Tsap, "Nonlinear finite element methods for nonrigid motion analysis," in *Proc. IEEE Workshop on Physics-Based Modeling in Computer Vision*, Cambridge, MA, June 1995, pp. 85–91.

[14] L. V. Tsap, D. B. Goldgof, and S. Sarkar, "Human skin and hand motion analysis from range image sequences using nonlinear FEM," in *IEEE Nonrigid and Articulated Motion Workshop*, San Juan, Puerto Rico, June 1997, pp. 80–89.

[15] L. V. Tsap, D. B. Goldgof, S. Sarkar, and W.-C. Huang, "Efficient nonlinear FEM modeling of nonrigid objects via optimization of mesh models," *Comput. Vision, Image Understanding: Special issue on CAD-Based Comput. Vision*, vol. 69, no. 3, pp. 330–350, Mar. 1998.

[16] M. Kass, A. Witkin, and D. Terzopoulos, "Snakes: active contour models," *Int. J. Comput. Vision*, vol. 1, no. 4, pp. 321–331, 1988.

[17] D. Terzopoulos and K. Waters, "Analysis of facial images using physical and anatomical models," in *Proc. IEEE 3rd Int. Conf. Computer Vision*, 1990, pp. 727–732.

[18] ——, "Analysis and synthesis of facial images using physical and anatomical models," *IEEE Trans. Pattern Anal. Machine Intell.*, vol. 14, pp. 569–579, June 1993.

[19] F. Leymarie and M. D. Levine, "Tracking deformable objects in the plane using an active contour model," *IEEE Trans. Pattern Anal. Machine Intell.*, vol. 15, pp. 617–634, June 1993.

[20] S. Kumar and D. B. Goldgof, "Automatic tracking of SPAMM grid and the estimation parameters from Cardiac MR images," *IEEE Trans. Med. Imag.*, vol. 13, pp. 122–132, Mar. 1994.

[21] L. D. Cohen and I. Cohen, "Deformable models for 3-D medical images using finite elements and balloons," in *Proc. IEEE CS Conf. Computer Vision and Pattern Recognition*, 1992, pp. 592–598.

[22] T. McInerney and D. Terzopoulos, "A finite element model for 3-D shape reconstruction and nonrigid motion tracking," in *Proc. 12th ICPR*, 1993, pp. 518–523.

[23] L. D. Cohen and I. Cohen, "A finite element method applied to new active contour models and 3-D reconstruction from cross sections," in *Proc. IEEE 3rd Int. Conf. Computer Vision*, 1990, pp. 587–591.

[24] ——, "Finite-element methods for active contour models and balloons for 2-D and 3-D images," *IEEE Trans. Pattern Anal. Machine Intell.*, vol. 15, pp. 1131–1147, Nov. 1993.

[25] J. C. McEachen, II, and J. S. Duncan, "Shape-based tracking of left ventricular wall motion," *IEEE Trans. Med. Imag.*, vol. 16, pp. 270–283, June 1997.

[26] A. Amini, R. Curwen, and J. Gore, "Snakes and splines for tracking nonrigid heart motion," *Lecture Notes in Comput. Sci.*, vol. 1065, pp. 252–261, 1996.

[27] D. Androutsos, P. E. Trahanias, and A. N. Venetsanopoulos, "Application of active contours for photochromic tracer flow extraction," *IEEE Trans. Med. Imag.*, vol. 16, pp. 284–293, June 1997.

[28] S. R. Gunn and M. S. Nixon, "A robust snake implementation; a dual active contour," *IEEE Trans. Pattern Anal. Machine Intell.*, vol. 19, pp. 63–68, Jan. 1997.

[29] H. D. Tagare, "Deformable 2-D template matching using orthogonal curves," *IEEE Trans. Med. Imag.*, vol. 16, pp. 108–117, 1997.

[30] A. Yezzi, Jr., S. Kichenassamy, A. Kumar, P. Olver, and A. Tannenbaum, "A geometric snake model for segmentation of medical imagery," *IEEE Trans. Med. Imag.*, vol. 16, pp. 199–209, Apr. 1997.

[31] N. Peterfreund, "The velocity snake," in *Proc. IEEE Nonrigid and Articulated Motion Workshop*, San Juan, Puerto Rico, June 1997, pp. 70–79.

[32] T. Sullivan J. Smith, J. Kermode, E. McIver, and D. J. Courtemanche, "Rating the burn scar," *J. Burn Care, Rehab.*, vol. 11, pp. 256–260, 1990.

[33] Y. C. Fung, *Biomechanics: Mechanical Properties of Living Tissues*, 2nd ed. New York: Springer-Verlag, 1993.

[34] W. F. Larrabee and J. A. Galt, "A finite element model of skin deformation. iii. the finite element model," *Laryngoscope*, vol. 96, pp. 413–419, Apr. 1986.

[35] W. F. Larrabee, "A finite element model of skin deformation. i.

[36] J. A. Weiss, J. A. Painter, and E. P. France, "Finite element mesh generation of the knee and its soft tissues from CT data," in *Proc. 2nd World Congress of Biomechanics*, Amsterdam, The Netherlands, July 1995, p. 149.

[37] F. Kallel and M. Bertrand, "Tissue elasticity reconstruction using linear perturbation method," *IEEE Trans. Med. Imag.*, vol. 15, pp. 299–313, June 1996.

[38] B. M. Chu and G. Brody, "Nondestructive measurements of the properties of healing burn scars," *Med. Instrum.*, vol. 9, pp. 139, 1975.

[39] W. F. Larrabee and D. Sutton, "A finite element model of skin deformation. ii. an experimental model of skin deformation," *Laryngoscope*, vol. 96, pp. 406–419, Apr. 1986.

[40] T. H. Bartell, W. W. Monafo, and T. A. Mustoe, "A new instrument for serial measurements of elasticity in hypertrophic scar," *J. Burn Care, Rehab.*, pp. 657–660, 1988.

[41] G. Esposito, P. Ziccardi, M. Scioli, N. Pappone, and N. Scuderi, "The use of a modified tonometer in burn scar therapy," *J. Burn Care, Rehab.*, vol. 11, pp. 86–90, 1990.

[42] R. Richard, J. Ford, S. F. Miller, and M. Staley, "Photographic measurement of volar foreman skin movement with wrist extension: The influence of elbow position," *J. Burn Care, Rehab.*, vol. 15, pp. 58–61, 1994.

[43] D. Smith Jr., "Use of biobrane in wound management," *J. Burn Care, Rehab.*, vol. 16, no. 3, pp. 317–320, 1995.

[44] R. Paul, J. Tarlton, P. Purslow, T. Sims, P. Watkins, F. Marshall, M. Ferguson, and A. Bailey, "Biomechanical and biochemical study of a standardized wound healing model," *Int. J. Biochem. Cell Biol.*, vol. 29, no. 1, pp. 211–220, Jan. 1997.

[45] H. Lafrance, L. Yahia, L. Germain, M. Guillot, and F. Auger, "Study of the tensile properties of living skin equivalents," *Biomed. Mater. Eng.*, vol. 5, no. 4, pp. 195–208, 1995.

[46] L. V. Tsap, D. B. Goldgof, S. Sarkar, and P. Powers, "Experimental results of a vision-based burn scar assessment technique," in *Proc. IEEE Workshop on Biomedical Image Analysis (WBIA'98)*, Santa Barbara, CA, June 1998, pp. 193–201.

[47] D. J. Williams and M. Shah, "A fast algorithm for active contours and curvature estimation," *CVGIP: Image Understanding*, vol. 55, no. 1, pp. 14–26, 1992.

[48] J. R. Brauer, *What Every Engineer Should Know About Finite Element Analysis*. New York: Marcel Dekker, 1993.

[49] *ANSYS User's Manual for Revision 5.3*, Swanson Analysis System, Inc., Houston, PA, 1996.

[50] D. S. Burnett, *Finite Element Analysis*. Reading, MA: Addison-Wesley, 1988.

[51] L. V. Tsap, D. B. Goldgof, and S. Sarkar, "Nonrigid motion analysis based on dynamic refinement of finite element models," in *Proc. IEEE CS Conf. Computer Vision and Pattern Recognition*, Santa Barbara, CA, June 1998, pp. 728–734.

[52] W. H. Press, B. P. Flannery, S. A. Teukolsky, and W. T. Vetterling, *Numerical Recipes in C: The Art of Scientific Programming*. Cambridge, U.K.: Cambridge Univ. Press, 1988.

[53] A. M. McIvor, "The accuracy of range data from a structured light system," Industrial Res. Ltd., Aukland, Tech Rep. 190: May 1994.

[54] *The Columbia University College of Physicians and Surgeons Complete Home Medical Guide*. New York: Crown, 1995.

[55] B. A. Todd and J. G. Thacker, "Three-dimensional computer model of the human buttocks, *in vivo*," *J. Rehab. Res.*, vol. 31, no. 2, pp. 111–119, 1994.

[56] M. B. Silver-Thorn, J. W. Steege, and D. S. Childress, "A review of prosthetic interface stress investigations," *J. Rehab. Res., Develop.*, vol. 33, no. 3, pp. 253–266, 1996.

[57] W. M. Vannah and D. S. Childress, "Modeling the mechanics of narrowly contained soft tissues: The effects of specification of Poisson's ratio," *J. Rehab. Res., Develop.*, vol. 30, no. 2, pp. 205–209, 1993.

[58] M. Zhang, M. Lord, A. R. Turner-Smith, and V. C. Roberts, "Development of a nonlinear finite element modeling of the below-knee prosthetic socket interface," *Med. Eng. Phys.*, vol. 17, no. 8, pp. 559–566, 1995.

[59] T. Maeno, K. Kobayashi, and N. Yamazaki, "Effect of geometry and property of the finger tissue on stress/strain distribution near the tactile receptors," in *Proc. 10th Conf. of the European Society of Biomechanics*, 1996, p. 312.

[60] C. W. J. Oomens, "A mixture approach to the mechanics of skin and subcutis," Ph.D. Thesis, Technische Hogeschool Twente, the Netherlands, 1985.

[61] J. G. Thacker, "The elastic properties of human skin *in vivo*," Ph.D. dissertation, Univ. of Virginia, Charlottesville, VA, 1976.